Corrosion Science xxx (2016) xxx–xxx

Contents lists available at ScienceDirect

Corrosion Science

journal homepage: www.elsevier.com/locate/corsci

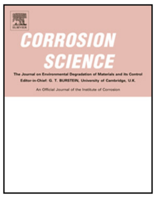

Size-dependent role of S phase in pitting initiation of 2024Al alloy

J. Wang, B. Zhang*, B. Wu, X.L. Ma

Shenyang National Laboratory for Materials Science, Institute of Metal Research, Chinese Academy of Sciences, 110016 Shenyang, China

ARTICLE INFO

Article history:
Received 25 September 2015
Received in revised form 12 January 2016
Accepted 13 January 2016
Available online xxx

Keywords:
A. Al alloy
B. STEM
C. Pitting corrosion

ABSTRACT

Size-dependent electrochemical role of the S phase at the initial corrosion stage of 2024Al alloy has been elucidated by transmission electron microscopy technique. A critical size of about 10 nm is identified below which S phases are out of electrochemical function at the initial corrosion stage, when $Al_{20}Cu_2Mn_3$ dispersoids play a crucial role. The electrochemical function of S phases becomes remarkable and triggers the local dissolution of the Al matrix with increasing the size. Moreover, the mechanism of the size effect has been discussed in detail.

1. Introduction

Al–Cu–Mg alloys are widely used in aerospace and other industrial applications due to the desirable combination of strength, damage tolerance, formability and density. The heterogeneous microstructure that consists of hardening precipitates and dispersoids is the main strengthening source of the Al–Cu–Mg alloys [1,2]. However, these precipitates and dispersoids also render the alloy prone to localized corrosion, hence premature breakdown may happen when they are utilized in a chloride containing environment [3–11]. In the last a few decades, researchers have been striving to study the pitting of 2024Al alloy which is a typical Al–Cu–Mg alloy. Among various second phase particles, attention is usually paid to the coarse S-Al_2CuMg phase, which is believed to dissolve preferentially as the initiation sites of pitting corrosion [12–20]. Due to the generally accepted opinion that the tiny precipitates or inclusions are less injurious than coarse ones, the effect of the nanometer-sized $Al_{20}Cu_2Mn_3$ dispersoids on pitting had been ignored until our recent work [21]. We have found that the micro-sized coarse S phases are embedded with nanosized $Al_{20}Cu_2Mn_3$ approximants of the decagonal quasicrystal. The $Al_{20}Cu_2Mn_3$ dispersoids, responsible for the heterogeneous activity of the S phase, are dissolved prior to the dissolution of S phase and subsequently trigger the dissolution of the adjacent S phase, ultimately creating macro pits at S phase. The prominent effect of the $Al_{20}Cu_2Mn_3$ phase is to indirectly influence the localized corrosion behavior of Al alloy by increasing the electrochemical activity of the S phase instead of directly impacting the Al matrix.

Extensive investigations have shown that heat treatment can modify the microstructure of Al alloys and yield diverse mechanical and corrosion properties [22–24]. In practical application, the nanometer-sized S phase precipitates which are key strengthening precipitates in high-strength Al–Cu–Mg alloys, are more frequently formed during precipitation heat treatment processes, where the S phase and $Al_{20}Cu_2Mn_3$ dispersoids are preferentially and separately distributed in the matrix, without being embedded. Under such conditions, the "self-catalyzing" process [21] which occurs specifically in coarse S phase and the embedded $Al_{20}Cu_2Mn_3$ dispersoids is no longer feasible. In such a distribution, clarifying the electrochemical role of the two types of second phase particles at the initial stages of corrosion is key to a comprehensive understanding of the mechanism of pitting initiation of 2024Al. However, the dissolution of nanometer-sized S phase precipitates is not attracting much attention. Birbilis et al. [25] using TEM observed that dissolution can occur on the nanometer-sized S phase. Ralstont et al. [26] obtained Al-2.5Cu-1.5Mg alloys with varied precipitate sizes at nanometer scale by various aging times, and measured their yield strength as a function of aging time. They illustrated that there exists a critical S precipitates size range, where the inverse correlation between strength and corrosion resistance is broken. And also implied that the microstructural features should be responsible for the initial hardening but being not harmful to the corrosion resistance. Regrettably, they did not clarify the second phase category which plays the main electrochemical role in this case.

The effect of the coarse precipitates/constitutes or inclusions with micrometer size on the corrosion properties of alloys could be readily clarified through traditional analysis tools with lower

---

* Corresponding author.
E-mail address: bozhang@imr.ac.cn (B. Zhang).

http://dx.doi.org/10.1016/j.corsci.2016.01.016
0010-938X/

Table 1
The evolution of the electrochemical role of S phase with size.

	Heat treatment temperature	Size of S phase	Coverage state of S phase by oxide film	Electrochemical role of S phase in initial corrosion
1	210 °C	2–10 nm	Totally covered	No role
2	270 °C	10–30 nm	Partially covered	Secondary role
3	350 °C	30–100 nm	Uncovered	Primary role

spatial resolution. Comparatively, the electrochemical role of the nanometer-sized counterparts is more difficult to distinguish due to the challenges of in-situ observation at nanometer scale; hence there is comparatively scant information available. In this study, the electrochemical role of the nanometer-sized S phase during the initial corrosion stage of 2024Al alloy, including the mechanism of the size-dependent effect, has been investigated by means of TEM (transmission electron microscopy) technique with HAADF (high angle annular dark field) mode.

2. Experimental procedure

2024Al alloy with nominal composition of Al-4.35Cu-1.55Mg-0.53Mn-0.11Fe-0.13Si-0.03Ti (wt.%) was chosen for this investigation. The solution treatments were performed at 495 °C. In order to obtain variant types of S phase with various sizes, three samples were subjected to varying heat treatments (at 210 °C, 270 °C and 350 °C, respectively) for 2 h. The samples were then prepared into TEM specimens. The TEM sample preparation procedure has been described in our previous published work [21] and also is presented briefly as follows. The heat-treated samples were first cut into sections using a linear precision saw with the thickness of 600 μm and ground to about 100 μm thicknesses by 1000 grit silicon carbide papers. Disks with diameter of 3 mm were prepared by die-cutting, then ground using variant grit silicon carbide papers, polished with diamond paste to 20 μm, and finally thinned by ion-milling. The specimens were immersed into neutral 0.5 mol/L NaCl solution at room temperature for various durations, cleaned in distilled water, dried, plasma-cleaned and then transferred into the TEM for investigation. Based on our observations, a suitable immersion time of about 10 min was selected, when the corrosion dissolution had begun but not propagated significantly. In the subsequent experimental investigation, all TEM specimens were firstly immersed in 0.5 mol/L NaCl solution for 10 min, then were observed further in TEM focusing on the locations where corrosion dissolution initiated.

A Tecnai G^2 F30 TEM and a Titan G^2 60-300Cs-corrected TEM, equipped with a HAADF detector and EDS (X-ray energy dispersive spectrometer) systems, were used at 300 kV in the present study.

3. Results and discussion

3.1. The distribution of nanometer-sized S precipitates

Fig. 1 is the HAADF image showing the distribution of second phase particles corresponding to the different heat treatment temperatures. The second phases, having brighter contrast, can be readily distinguished by their needle shaped and rod shaped morphologies. The rod-like phase with width of about 100 nm is the $Al_{20}Cu_2Mn_3$ section, which is known to form during the homogenization process and keeps good thermal stability in subsequent heat treatments, hence have almost unvaried size (Fig. 1a–c). The needle-shaped phase, which is mostly the nanometer-sized S precipitate section (in addition to some θ (Al_2Cu) phases) reflect size variation with heat treatment temperature. Hence, nano-sized S phase with variant sizes was obtained via the heat treatment regime, and successfully distinguished from the $Al_{20}Cu_2Mn_3$ phase. Fig. 1a shows the fine needle-shaped S phase precipitates obtained after 2 h heat treatment at 210 °C to have widths ranging from 2 to 10 nm. Increasing the heat temperature to 270 °C caused the width of needle-shaped S precipitates to increase to 10–30 nm as shown in Fig. 1b. The 350 °C heat treatment yielded larger lath-shaped S precipitates of width 30–100 nm. Fig. 1d is the high resolution STEM image of the S phase along the [100] zone axis, in which the direction of the S [100] is parallel to the Al [100].

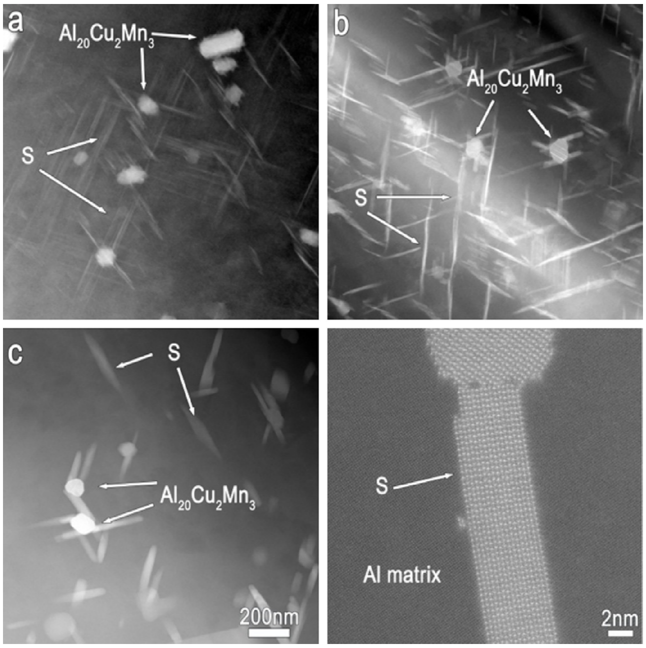

Fig. 1. The HAADF images showing the distribution of second phase particles in 2024Al alloy after aging treatment for 2 h at various temperatures of 210 °C (a), 270 °C (b) and 350 °C (c). (d) High resolution STEM image of S-Al_2CuMg phase along [100] zone axis (S [100]//Al [100]) in the 2024Al alloy aged at 270 °C.

3.2. The size-dependent electrochemical role of S phase in the initial corrosion stage

After immersion in 0.5 mol/L NaCl solution for 10 min, the three types of samples were observed in HAADF-STEM mode. The HAADF-STEM mode provides incoherent images which collects high-angle scattered electrons and yields to strong atomic number (Z) contrast. Therefore, the image contrast in such a mode is strongly associated with the local variety of chemical composition and/or thickness contribution [27]. Local dissolution can thus result in a darker contrast in such a mode. Fig. 2 is the HAADF image showing the local dissolution of the sample treated at 210 °C corresponding to the S precipitates size of 2–10 nm. Several small pits with diameter of 200–400 nm are obvious, which have darker contrast owing to local dissolution. There exists a core with diameter of several tens of nanometers in each pit, which can be distinguished from the distinct morphology of the dissolved remnant, as shown in Fig. 2b I–II. The EDS mapping analysis was performed on such a pit (Fig. 3a) to further identify the precursor of the core. The maps of the elements O, Cu, Al, Mn and Mg are shown in Fig. 3b–f. It can be seen that the elements Cu and Mn still remain within the remnant core, which combined with the rod-shaped morphology, indicates

Please cite this article in press as: J. Wang, et al., Size-dependent role of S phase in pitting initiation of 2024Al alloy, *Corros. Sci.* (2016), http://dx.doi.org/10.1016/j.corsci.2016.01.016

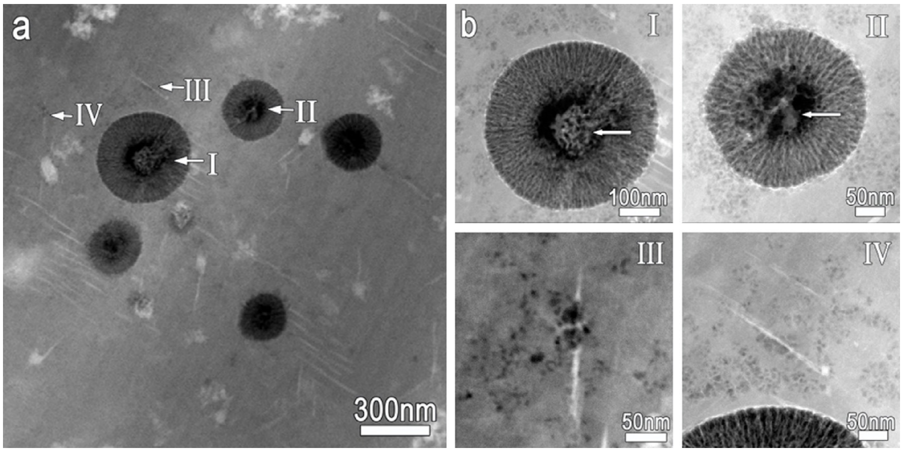

Fig. 2. The HAADF images showing the local dissolution of the sample treated at 210 °C corresponding to the S precipitates size of 2–10 nm. (a) Several pits with diameter of 200–400 nm are formed. A core with a diameter of several tens of nanometers is seen in each pit. Almost the S phases are free of corrosion. (b) Zoom in images in (a) labeled as I, II, III, and IV.

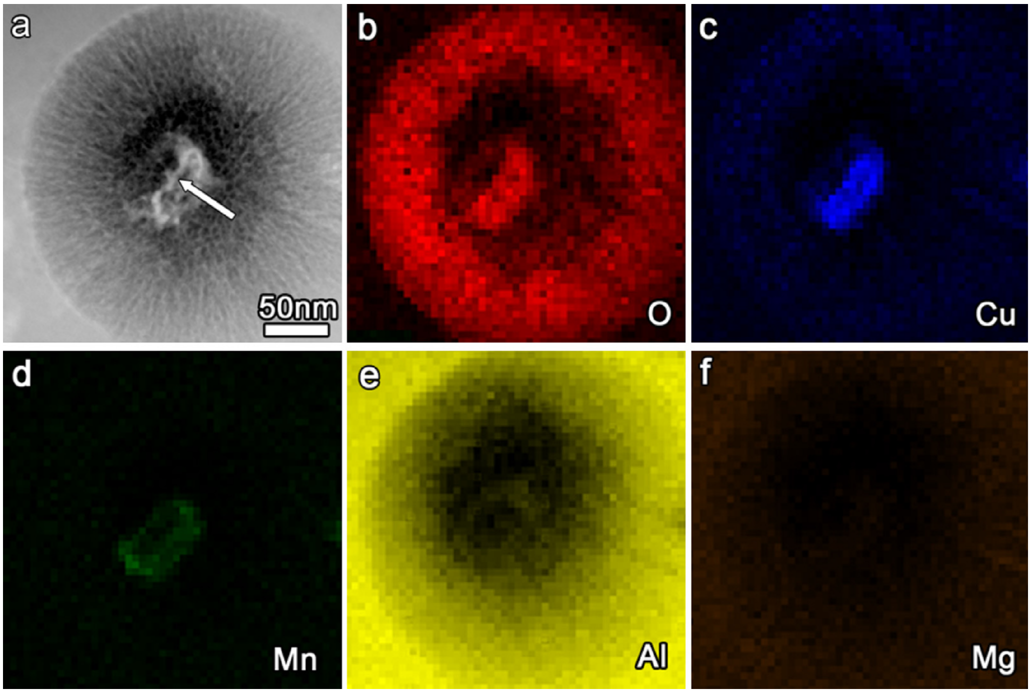

Fig. 3. EDS mapping analysis on a pit with the remnant core of $Al_{20}Cu_2Mn_3$ dispersoid. (a) HAADF image showing a pit. (b–f) Element maps of O, Cu, Mn, Al and Mg.

that the precursor of the core should be $Al_{20}Cu_2Mn_3$. The enrichment in O element should result from the hydrolysis of selectively dissolved Al cations. Comparatively, it is hard to find dissolution in the needle-shaped S phase and its surrounding Al matrix. At a higher resolution, only very slight dissolution was found on few of the S needles and some trace-dissolution dots are as well observed to distribute over the adjacent matrix, as shown in Fig. 2b III–IV, which corresponds to a minor anodic process. Evidently, when the nanosized S phase have width of 2–10 nm, the $Al_{20}Cu_2Mn_3$ dispersoids directly impact the Al matrix and play the major role in triggering pitting corrosion. The observation indicates that only the $Al_{20}Cu_2Mn_3$ dispersoids play the key electrochemical role in such a size range. Instead of the fine S phase, the $Al_{20}Cu_2Mn_3$ phase is the primary or even only determinant of the macro corrosion properties. The dispersoids are known to maintain good thermal stability during heat treatment; as a result, the corrosion properties are expected to be stable in the critical size range.

Fig. 4 is the HAADF image showing the local dissolution of the sample treated at 270 °C, corresponding to the S precipitates size of 10–30 nm. Similarly, some small pits resulting from local dissolution are obvious and a remnant core of $Al_{20}Cu_2Mn_3$ was also found in each pit. Interestingly, besides the $Al_{20}Cu_2Mn_3$ remnant, the remnant of dissolved S needles was also found in the pit, which cross-linked with the dissolved $Al_{20}Cu_2Mn_{3,}$ as shown in Fig. 4b (I–III). The EDS mapping analysis on such a pit is shown in Fig. 5. Fig. 5a is the HAADF image of a small pit with a dissolved remnant core. The maps of O, Cu, Al, Mn and Mg in Fig. 5b–f shows the rod-shaped core to be enriched in Mn and Cu and the needle-shaped core enriched in Cu. The EDS result further revealed the rod-shaped core to be the remnant of $Al_{20}Cu_2Mn_3$ in which Al dissolved preferentially, and the needle-shaped core the remnant of S-Al_2CuMg in which Al and Mg dissolved preferentially. Meanwhile, individual S needles, not cross-linked with the $Al_{20}Cu_2Mn_3$ dissolved slightly and caused the slight dissolution of the adjacent

Please cite this article in press as: J. Wang, et al., Size-dependent role of S phase in pitting initiation of 2024Al alloy, *Corros. Sci.* (2016), http://dx.doi.org/10.1016/j.corsci.2016.01.016

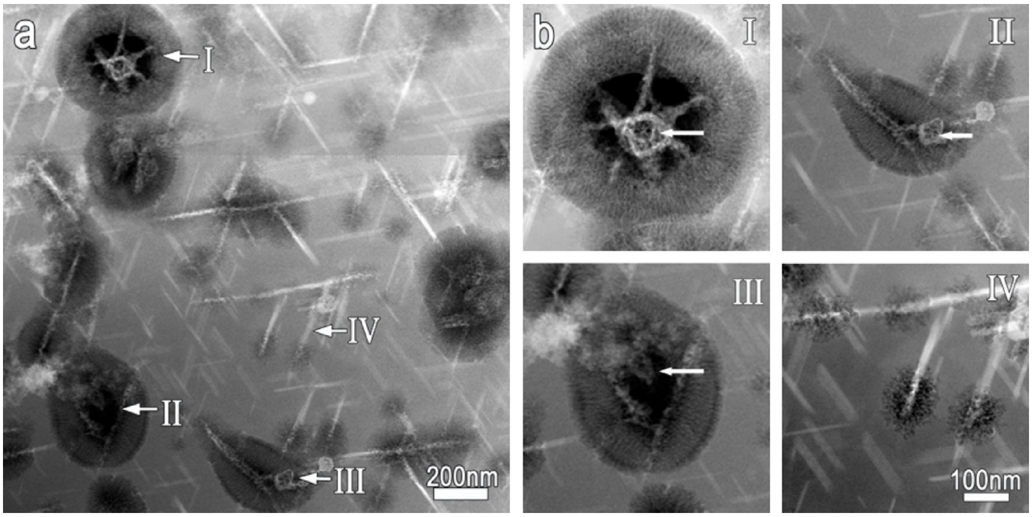

Fig. 4. The HAADF images showing the local dissolution of the sample treated at 270 °C corresponding to the S precipitates size of 10–30 nm. (a) Some pits resulted from the local dissolution are left behind. Besides the remnant core of $Al_{20}Cu_2Mn_3$, the remnant of dissolved S needles also can be found in the pit. The slightly local dissolution of Al matrix is triggered by the separated S needles. (b) Zoom in images in (a) labeled as I, II, III, and IV.

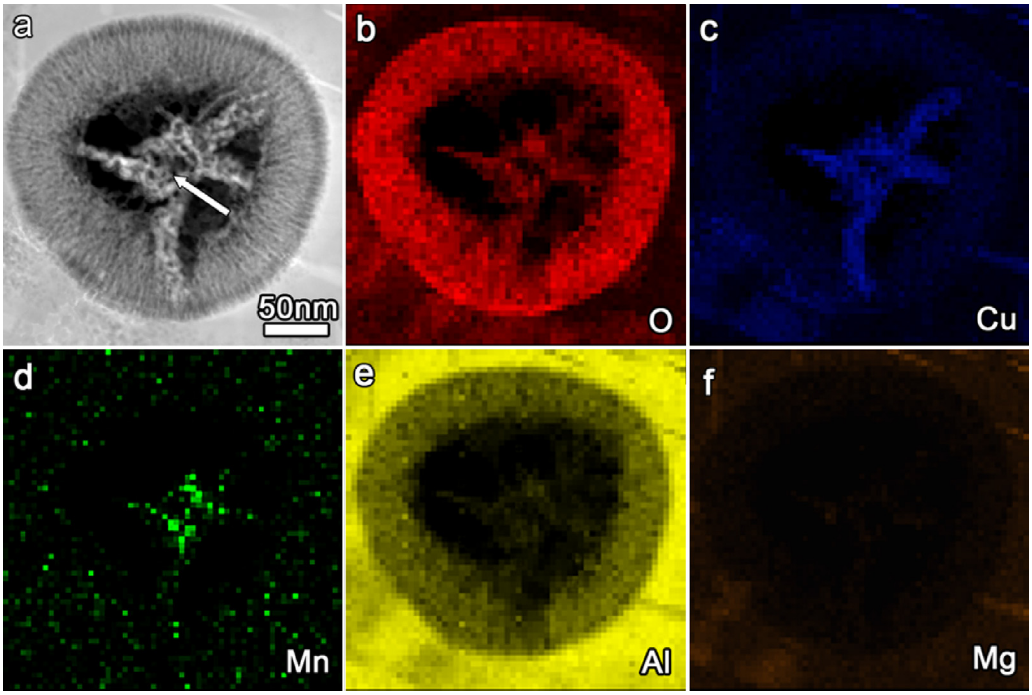

Fig. 5. (a) HAADF image showing a pit with the remnant core of partially dissolved $Al_{20}Cu_2Mn_3$ and several S needles. (b–f) Element maps of O, Cu, Mn, Al and Mg.

Al matrix, as shown in Fig. 4a and bIV. Nonetheless, the pits formed by only S precipitates were much smaller than those formed by $Al_{20}Cu_2Mn_3$ particles. This means that although the 10–30 nm sized S precipitates begin to take part in the initial corrosion process, they only play a secondary role in the electrochemical activity. Therefore, the pits form preferentially at the $Al_{20}Cu_2Mn_3$ particles and then at the S precipitates. The initial pitting is still dominated by the dissolution of $Al_{20}Cu_2Mn_3$.

Comparison of Figs. 2 and 4 reveals another interesting phenomenon, wherein the small dissolution pits have circular shapes on the sample treated at 210 °C, but are quite irregular for the sample treated at 270 °C, which is another manifestation of the size-dependent role of S phase. The S precipitates with size of 2–10 nm have no noticeable effect on the corrosion dissolution process, hence the pits occurred at the $Al_{20}Cu_2Mn_3$ dispersoids and propagated homogeneously around the remnant core, yielding the circular pits (Fig. 2). The electrochemical role of the S phase particles became important when the widths reach 10–30 nm, with pits formed under the synergistic effect of the S and $Al_{20}Cu_2Mn_3$ phases propagating along the needle shaped S precipitates, yielding irregular appearance. The one near regular pit observed under this condition is seen from Fig. 4 (arrowed with I) to involve several S needles connected radially in one $Al_{20}Cu_2Mn_3$ dispersoid, thus the pit extends radially to a near circular outline.

On further increasing the heat treatment temperature to 350 °C, relatively coarse S precipitates with width of 30–100 nm were obtained. Similarly, the characters in the initial corrosion were observed. As shown in Fig. 6, more pits were formed on the sample treated at 350 °C. Besides several relatively big and deep pits formed around some S phase and $Al_{20}Cu_2Mn_3$ dispersoids, many

Please cite this article in press as: J. Wang, et al., Size-dependent role of S phase in pitting initiation of 2024Al alloy, *Corros. Sci.* (2016), http://dx.doi.org/10.1016/j.corsci.2016.01.016

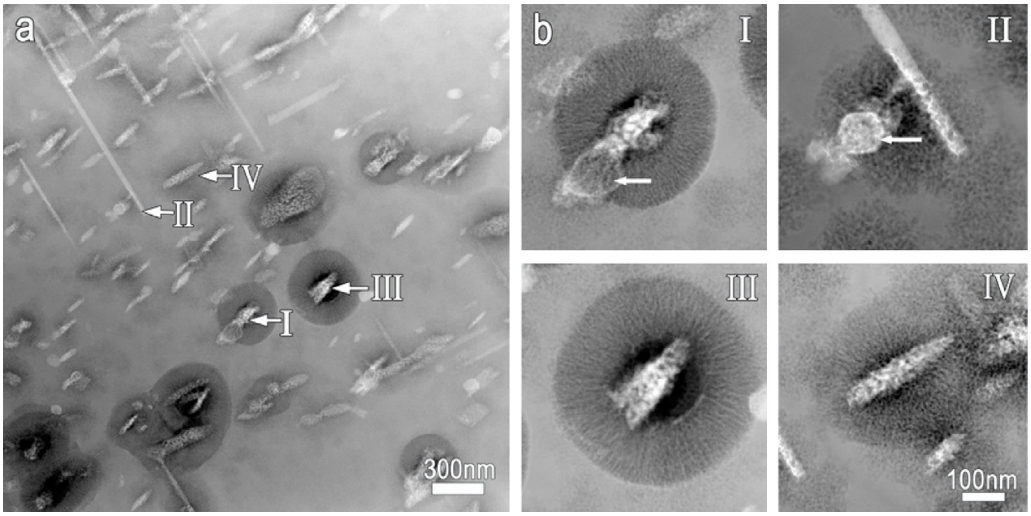

Fig. 6. The HAADF images showing the local dissolution of the sample treated at 350 °C corresponding to the S precipitates size of 30–100 nm. (a) pits are formed around, almost dispersed $Al_{20}Cu_2Mn_3$ and lath like S precipitates (b) Zoom in images of the dissolution in (a) labeled as I, II, III, and IV.

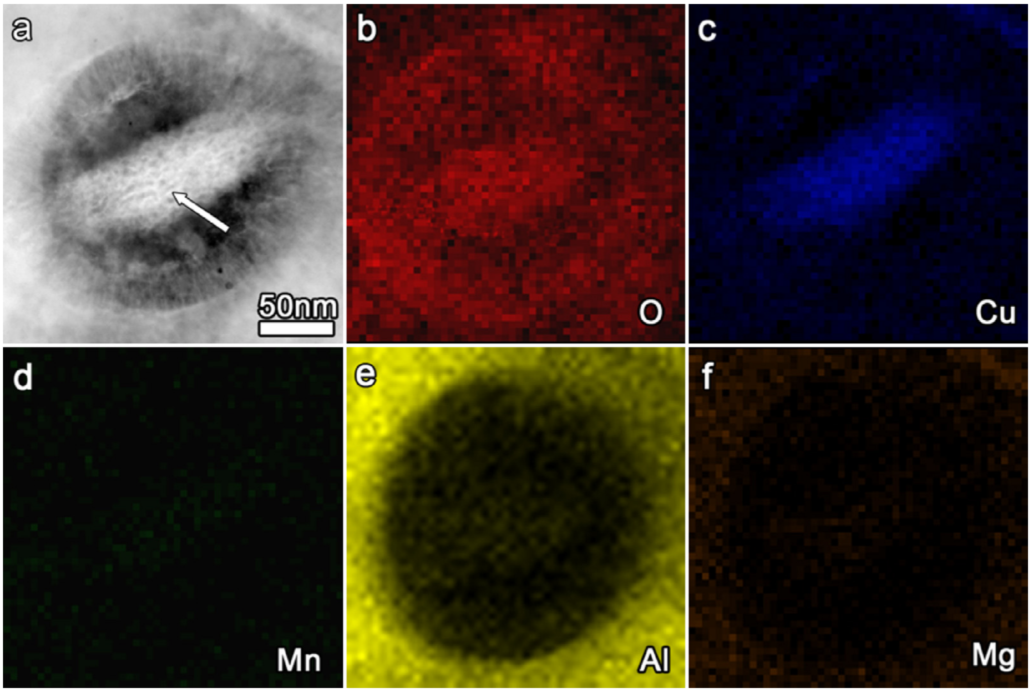

Fig. 7. (a) HAADF image showing of a pit with the remnant core of S-Al_2CuMg particle. (b–f) Element maps of O, Cu, Mn, Al and Mg.

slight and shallow pits can be seen at almost all the S precipitates. Fig. 6b is the zoom in image showing the four pits arrowed in Fig. 6a. In the pits I and II, the cores are the combined remnants of the $Al_{20}Cu_2Mn_3$ and S precipitates. However, the cores in pits III and IV are only the remnants of the S phase, which means the lath shaped S precipitates with size of 30–100 nm can initiate dissolution of the Al matrix and form pits independently. This confirms that the electrochemical role of the S phase becomes significant with increasing size. Fig. 7 shows the EDS mapping result of the pit formed around the S phase. It is seen that selective dissolution of elements Al and Mg occurs in the S phase, leaving a Cu-rich remnant.

To sum-up, the fine S precipitates with width <10 nm had negligible electrochemical role, particles with sizes in the range 10–30 nm played a secondary role, while particles >30 nm exerted pronounced effects on the electrochemical activity, as illustrated in Table 1. Hence, the electrochemical role of S phase particles on the initial dissolution of the 2024Al alloy is size-dependent and becomes prominent with increasing size.

3.3. *The possible mechanism on the size-dependent electrochemical role of S phase*

As aforementioned, the electrochemical role of S phase is size-dependent and becomes prominent with increasing size, which seems like conflict with the long-standing theory of “large cathode/small anode couple”, e.g. the smaller the anodic components and the larger the cathodic components, the more severe the corrosion. Interestingly, the small S phase with size of 2–10 nm is actually free of corrosion at the initial stage, and seems to play a cathodic role. The reversed role may be ascribed the relationship between the S phase particle size and the integrity of the protective passive film on the aluminium matrix. The coarse precipitates and

Please cite this article in press as: J. Wang, et al., Size-dependent role of S phase in pitting initiation of 2024Al alloy, *Corros. Sci.* (2016), http://dx.doi.org/10.1016/j.corsci.2016.01.016

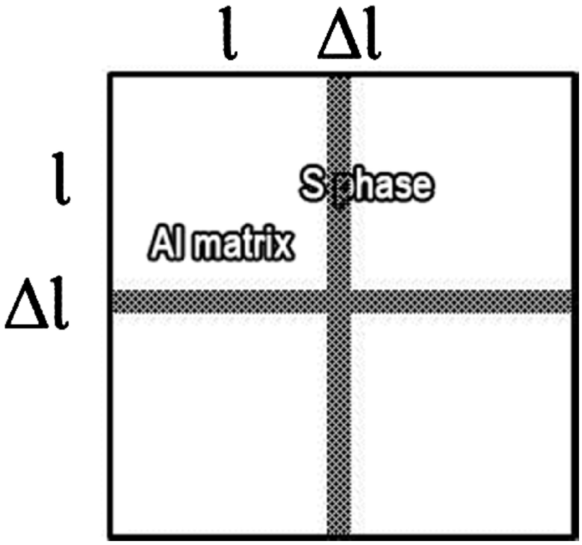

Fig. 8. The simplified schematic diagram showing the cross-shaped distribution of S-Al_2CuMg phase.

dispersoids could render the passive film discontinuous, with the exposed anodic components, such as the S phase and $Al_{20}Cu_2Mn_3$ dispersoids, dissolving preferentially. Unlike the situation when the S phase is very thin, it can be covered by the passive film and thus plays the reverse (cathodic) role. The value of Pilling–Bedworth ratio (e.g. R_{PBR}, volume per metal ion in the oxide: volume per metal atom in the metal) for Al_2O_3/Al is about 1.20, as calculated using the PBR formula (Eq. 1) whereas the literature reported a value of about 1.65 [28]. In other words, $R_{PBR} > 1$ means that the film can totally cover the Al matrix. When $R_{PBR} > 1$, compressive stress exists in the oxide film, which induces an expansive trend in the film. For the isotropic oxide film, the volume strain (ε_V) obtained from the R_{PBR} is expressed approximately as:

$$\varepsilon_V = 1 - R_{PBR}{}^{1/3}(1)$$

The R_{PBR} of aluminum oxide is assigned as 1.65, yielding a calculated volume strain of about 18%, e.g. $\Delta V/V = 18\%$; where V is the volume of the Al matrix in some zone, and ΔV is the volume expansion when the Al is oxidized to oxide. As shown in Fig. 1, the S phase needles lie across each other, which is further simplified in the schematic shown in Fig. 8. l is the distance between two parallel S needles. Δl is the linear expansion along x and y direction. Here, it is assumed that the volume expansion is only along x and y direction and the strain released totally. Accordingly,

$$\frac{\Delta V}{V} = \frac{\Delta A}{A} = \frac{(l+\Delta l)^2 - l^2}{(l+\Delta l)^2} = 18\% \tag{2}$$

$$\frac{\Delta l}{l} \approx 0.1 \tag{3}$$

where A is the area of oxide and ΔA is the area expansion. According to Fig. 1, l (the distance between S phase needles), is about 40–100 nm at 210 °C, 100–200 nm at 270 °C and 200–300 nm at 350 °C. Correspondingly, Δl is 4–10 nm, 10–20 nm and 20–30 nm at the three temperatures above. In fact, the factual linear expansion should be a little smaller since the stress would not release totally but maintain a certain strain value. Evidently, when the S phase is small in one dimension, such as 2–10 nm obtained at 210 °C, the protective oxide film can totally cover the thin S phase particles through volume expansion, as illustrated in Fig. 9a. The film can bridge the S phase and Al matrix, which leads to the ennoblement in the potential of the S phase and thus S phases are free of corrosion at the initial stage. At 270 °C, when the S phase needles are 10–30 nm, smaller S phase particles can be covered and thus remain free of corrosion, while larger particles can only be covered partially (illustrated in Fig. 9b) and thus undergo dissolution at the exposed sites. This is consistent with the results in Fig. 4a, which shows some larger S phase needles to be dissolved and smaller remained unattacked. Comparatively, at 350 °C and S phase 30–100 nm, the oxide film cannot cover the S phase totally any longer through the volume expansion (Fig. 9c). Therefore, most of the S phases are dissolved as shown in Fig. 6a. It is noteworthy that the $Al_{20}Cu_2Mn_3$ with width about 100 nm cannot possibly be covered by the oxide film and as such always plays the leading role at the initial corrosion stage.

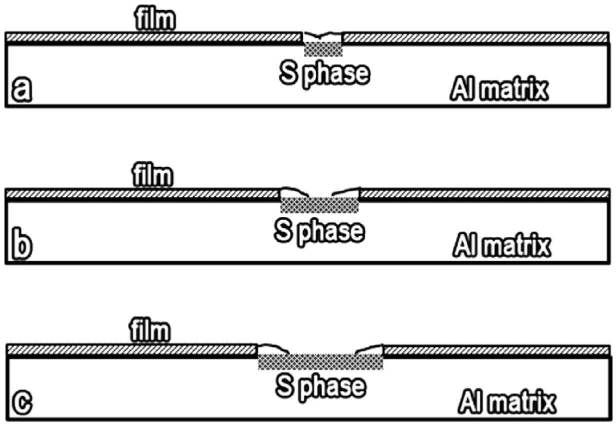

Fig. 9. Schematic diagram illustrating the oxide film coverage on the S-phase with increasing size.

The present study has important implications for alloy design strategies in application where corrosion properties are important.

4. Conclusions

The present study applied in-situ ex-environmental HAADF-STEM technique to clarify the size-dependent electrochemical role of the S phase at the initial corrosion stage of 2024Al alloy. A critical size of about 10 nm has been identified below which the S precipitates are free of corrosion and the pits are formed at $Al_{20}Cu_2Mn_3$ dispersoids. With increasing size, the electrochemical function of S phase becomes significant and triggers the local dissolution of the Al matrix. The size-dependent role is ascribed to oxide film expansion on the passive film coverage on the S phase.

Acknowledgements

This work is supported by the National Natural Science Foundation of China (51101157), the Innovation Fund in IMR (SCJJ-2013-PY-09) and the National Basic Research Program of China (2009CB623705). The authors are grateful to Prof. T. Zhang for fruitful discussions and Prof. E. E. Oguzie and Dr. S. Jagadeesh for suggestion and modification in English.

References

[1] S.C. Wang, M.J. Starink, Precipitates and intermetallic phases in precipitation hardening Al–Cu–Mg–(Li) based alloys, Int. Mater. Rev. 50 (2005) 193–215.
[2] S. Cheng, Y.H. Zhao, Y.T. Zhu, E. Ma, Optimizing the strength and ductility of fine structured 2024Al alloy by nano-precipitation, Acta Mater. 55 (2007) 5822–5832.
[3] B.B. Wang, Z.Y. Wang, W. Han, W. Ke, Atmospheric corrosion of aluminium alloy 2024-T3 exposed to salt lake environment in Western China, Corros. Sci. 59 (2012) 63–70.
[4] J.A. DeRose, T. Suter, A. Balkowiec, J. Michalski, K.J. Kurzydlowski, P. Schmutz, Localised corrosion initiation and microstructural characterisation of an Al 2024 alloy with a higher Cu to Mg ratio, Corros. Sci. 55 (2012) 313–325.

Please cite this article in press as: J. Wang, et al., Size-dependent role of S phase in pitting initiation of 2024Al alloy, *Corros. Sci.* (2016), http://dx.doi.org/10.1016/j.corsci.2016.01.016

[5] C. Augustin, E. Andrieu, C. Blanc, G. Mankowski, J. Delfosse, Intergranular corrosion of 2024 alloy in chloride solutions, J. Electrochem. Soc. 154 (2007) C637–C644.

[6] G.O. Ilevbare, J.R. Scully, Mass-transport-limited oxygen reduction reaction on AA2024-T3 and selected intermetallic compounds in chromate-containing solutions, Corrosion 57 (2001) 134–152.

[7] S. Minhua, F. Yan, H. Ronggang, L. Changjian, A study on pitting corrosion of aluminum alloy 2024-T3 by scanning microreference electrode technique, Mater. Sci. Eng. A (Struct. Mater.: Prop. Microstruct. Process.) A344 (2003) 323–327.

[8] W.L. Zhang, G.S. Frankel, Transitions between pitting and intergranular corrosion in AA2024, Electrochim. Acta 48 (2003) 1193–1210.

[9] K. Kowal, J. DeLuccia, J.Y. Josefowicz, C. Laird, G.C. Farrington, In situ atomic force microscopy observations of the corrosion behavior of aluminum–copper alloys, J. Electrochem. Soc. 143 (1996) 2471–2481.

[10] N. Radutoiu, J. Alexis, L. Lacroix, M. Abrudeanu, J.-A. Petit, Application of kelvin probe force microscopy (KFM) to evidence localized corrosion of over-aged aeronautical 2024 aluminum alloy. In: Karama, M., Alexis, J. (Eds.), Behav. Mater. 550 (2013) 127–134.

[11] W. Qafsaoui, M.W. Kendig, H. Perrot, H. Takenouti, Effect of 1-pyrrolidine dithiocarbamate on the galvanic coupling resistance of intermetallics—aluminum matrix during corrosion of AA 2024-T3 in a dilute NaCl, Corros. Sci. 92 (2015) 245–255.

[12] A. Boag, A. Hughes, A. Glenn, T. Muster, D. McCulloch, Corrosion of AA2024-T3 Part I: localised corrosion of isolated IM particles, Corros. Sci. 53 (2011) 17–26.

[13] R. Buchheit, R. Grant, P. Hlava, B. McKenzie, G. Zender, Local dissolution phenomena associated with S phase (Al2CuMg) particles in aluminum alloy 2024-T3, J. Electrochem. Soc. 144 (1997) 2621–2628.

[14] V. Guillaumin, G. Mankowski, Localized corrosion of 2024 T351 aluminium alloy in chloride media, Corros. Sci. 41 (1999) 421–438.

[15] D.Q. Zhu, W.J. van Ooij, Corrosion protection of AA 2024-T3 by bis-3-(triethoxysilyl) propyl tetrasulfide in sodium chloride solution. Part 2: mechanism for corrosion protection, Corros. Sci. 45 (2003) 2177–2197.

[16] N. Birbilis, R.G. Buchheit, D.L. Ho, M. Forsyth, Inhibition of AA2024-T3 on a phase-by-phase basis using an environmentally benign inhibitor, cerium dibutyl phosphate, Electrochem. Solid State Lett. 8 (2005) C180–C183.

[17] M. Bethencourt, F.J. Botana, M.J. Cano, M. Marcos, J.M. Sanchez-Amaya, L. Gonzalez-Rovira, Behaviour of the alloy AA2017 in aqueous solutions of NaCl. Part I: corrosion mechanisms, Corros. Sci. 51 (2009) 518–524.

[18] A. Boag, R.J. Taylor, T.H. Muster, N. Goodman, D. McCulloch, C. Ryan, B. Rout, D. Jamieson, A.E. Hughes, Stable pit formation on AA2024-T3 in a NaCl environment, Corros. Sci. 52 (2010) 90–103.

[19] H. Shi, Z. Tian, T. Hu, F. Liu, E.-H. Han, M. Taryba, S.V. Lamaka, Simulating corrosion of Al2CuMg phase by measuring ionic currents, chloride concentration and pH, Corros. Sci. 88 (2014) 178–186.

[20] J. Li, N. Birbilis, R.G. Buchheit, Electrochemical assessment of interfacial characteristics of intermetallic phases present in aluminium alloy 2024-T3, Corros. Sci. 101 (2015) 155–164.

[21] J. Wang, B. Zhang, Y.T. Zhou, X.L. Ma, Multiple twins of a decagonal approximant embedded in S-Al2CuMg phase resulting in pitting initiation of a 2024Al alloy, Acta Mater. 82 (2015) 22–31.

[22] Y.C. Lin, Y.-Q. Jiang, Y.-C. Xia, X.-C. Zhang, H.-M. Zhou, J. Deng, Effects of creep-aging processing on the corrosion resistance and mechanical properties of an Al–Cu–Mg alloy, Mater. Sci. Eng.: A 605 (2014) 192–202.

[23] H. Min, R. Ji Gang, L. Ming, Z. Kun, W. Liang, F. Zhaohui, Microstructure evolution and mechanical properties of an Al–Cu–Mg alloy at elevated temperature, Adv. Mater. Res. 1004–1005 (2014) 148–153.

[24] N. Afzal, T. Shah, Microstructural features and mechanical properties of artificially aged AA2024, Strength Mater. 45 (2013) 684–692.

[25] N. Birbilis, M.K. Cavanaugh, L. Kovarik, R.G. Buchheit, Nano-scale dissolution phenomena in Al–Cu–Mg alloys, Electrochem. Commun. 10 (2008) 32–37.

[26] K.D. Ralston, N. Birbilis, M. Weyland, C.R. Hutchinson, The effect of precipitate size on the yield strength-pitting corrosion correlation in Al–Cu–Mg alloys, Acta Mater. 58 (2010) 5941–5948.

[27] S.J. Pennycook, Structure determination through Z-contrast microscopy, in: P.W. Hawkes (Ed.), Advances in Imaging and Electron Physics, Microscopy, Spectroscopy, Holography and Crystallography with Electrons, 123, Elsevier, 2002, pp. 173–206.

[28] K. Tzoganakou, P. Skeldon, G.E. Thompson, X. Zhou, U. Kreissig, E. Wieser, H. Habazaki, K. Shimizu, Mobility of lithium ions in anodic alumina formed on an Al–Li alloy, Corros. Sci. 42 (2000) 1083–1091.

Please cite this article in press as: J. Wang, et al., Size-dependent role of S phase in pitting initiation of 2024Al alloy, *Corros. Sci.* (2016), http://dx.doi.org/10.1016/j.corsci.2016.01.016